Effects of annealing time on the structure and optical properties of $ZnAl_2O_4$/ZnO prepared via citrate sol-gel process

Setumo Victor Motloung[1*], Pushpa Kumari[2], Lehlohonolo Fortune Koao[3], Tshwafo Elias Motaung[4], Thulani Thokozani Hlatshwayo[5], Mokgaotsa Jonas Mochane[4]

[1]Department of Physics, Sefako Makgatho Health Science University, P. O. Box 94, Medunsa, 0204, South Africa

[2]Department of Physics, National Institute of Technology, Kurukshetra, Haryana- 136119, India

[3]Department of Physics, University of the Free State (Qwaqwa Campus), Private Bag X13, Phuthaditjhaba, 9866, South Africa

[4]Department of Chemistry, University of Zululand, Private bag X 1041, Richards Bay, 3900, South Africa

[5]Department of Physics, University of Pretoria, Private Bag X 20, Hatfield, 0028, South Africa

*Corresponding authot. Tel: (+27) 729204758; E-mail: cchataa@gmail.com (Setumo Victor Motloung)

Abstract

$ZnAl_2O_4$ nano-powders have been successfully prepared via citrate sol-gel technique. All powder samples were annealed at 600 ^{o}C for 1, 2, and 3 h. Thermogravimetric analysis (TGA) confirmed that the minimum annealing temperature of crystallization is ~ 400 °C. Fourier Transform Infrared (FTIR) results showed a series of absorption peaks in the range of 810 - 4000 cm^{-1}. The X-ray diffraction (XRD), scanning electron microscopy (SEM) and high-resolution transmission electron microscopy (HR-TEM) results showed that the prepared nano-crystals consists of the mixture of both cubic ($ZnAl_2O_4$) and hexagonal (ZnO) structures. Ultra violet visible (UV-vis) spectroscopy revealed that the annealing time (AT) influences the band gap of the prepared phosphor materials. When the

samples were excited at 275 nm, two emission peaks at 428 nm (violet) and 561 nm (green-yellow) were observed and they are attributed to the defects levels within the ZnO and $ZnAl_2O_4$ band gaps. The Commission Internationale de l'Elcairage (CIE) colour coordinates confirmed that all the prepared samples exhibit the violet emission and varying the AT does not influence the emission colour.

1. Introduction

Over the past decades, spinel compounds have attracted interest in many researchers around the globe due to their properties such as high chemical and thermal stability, high mechanical resistance, low sintering temperature and high quantum yields [1,2]. Spinels are class of binary transition metal oxides of the form AB_2O_4 with varied structures and owing to their unique properties, they have found potential applications in the area of material science and technology [3,4]. Among the various spinel oxides available, zinc aluminate ($ZnAl_2O_4$), has gained lot of attention because of its multidisciplinary interest [4]. $ZnAl_2O_4$ has drawn much attention, as a result of its usefulness in ceramic, electronics, catalyst, catalyst support, aerospace, paint, dielectric and sensing applications [4-6]. $ZnAl_2O_4$ is a semiconductor material that is suitable for ultraviolet (UV) photoelectronic application. This is due to its wide bandgap energy ($E_g \sim 3.8$ eV), which also makes it suitable for an applications such as optical coating or host matrix of different phosphors materials [7,8]. Based on the above mentioned diverse applications of $ZnAl_2O_4$ spinel, various morphologies have been prepared, including one-dimensional microfibers, porous structures, nanoparticles, nanorods, nanotubes [8]. The luminescent properties of phosphors have been reported to strongly depend on the particle size, crystal structure, uniform distribution of activators in the host lattice, morphologies and preparation methods [8,9]. In particular, $ZnAl_2O_4$ nanostructures are expected to exhibit enhanced optical and

2

luminescence properties. Thus, much more efforts have been devoted to study the luminescent properties of the pure and impurities-doped $ZnAl_2O_4$ [10].

From the preparation point of view, the formation of $ZnAl_2O_4$ spinel has been obtained by different routes, such as co-precipitation [11], modified citrate [12], microwave-hydrothermal [13], solid-state reaction [14], hydrothermal [15], sol-gel [16] and polymeric precursor [17]. Compared with the traditional methods, the sol-gel route offers the advantages such as good stoichiometric control, high homogeneity, producing nanostructured powders and thin films, as well as low temperature processing [9]. In view of this and as an alternative, the sol-gel method was employed to synthesize the $ZnAl_2O_4$ nano-powders in this study. There are many other studies on the $ZnAl_2O_4$, which have been reported in literature. Most of these investigations or reports have focused more on the influence of doping concentrations [18], influence of annealing temperature [19,20] ,influence of different aluminium salts [8] and influence of citric acid (CA) content [21] on the morphology, structure and optical properties of the obtained $ZnAl_2O_4$ products. However, to the best of our knowledge, the effects of annealing time (AT) on the $ZnAl_2O_4$ preparation have not been investigated. Henceforth, in this context, the initial main aim of this work was to synthesize $ZnAl_2O_4$ nanoparticles by sol-gel method, which is subsequently followed by thermal treatment (annealing at constant temperature of 600 ^{o}C for various periods in air) in order to acquire more knowledge on the material properties and to evaluate their capabilities in the applications such as in the light emitting materials. The temperature of 600 ^{o}C was kept constant because in our previous results [19], it gave the highest PL emission intensity. Another objective is to identify or explore the optimum AT for the highest PL. The results showed that the final powder products consist of the impurities of hexagonal ZnO, which agrees very well with the findings in Ref [19]. Therefore, this paper investigates the effects of annealing time (AT) on the structure, morphology and optical properties of the $ZnAl_2O_4$/ZnO. The observed photoluminescence emission channel or pathways is also proposed.

2. Experimental details

2.1. Materials

Zn(NO$_3$)$_2$·6H$_2$O (98%), Al(NO$_3$)$_3$·9H$_2$O (98.5%) and citric acid (CA) C$_8$H$_8$O$_7$·H$_2$O (99%) were purchased from Laboratory Consumables & Suppliers cc, (South Africa) and they were used without further purification.

2.2. Synthesis

ZnAl$_2$O$_4$ nano-powders were synthesized using the well-known sol-gel technique [16] by dissolving specified amounts of Zn(NO$_3$)$_2$·6H$_2$O (98%), Al(NO$_3$)$_3$·9H$_2$O (98.5%) and citric acid (CA) C$_8$H$_8$O$_7$·H$_2$O (99%) in deionized water. The CA was used as a complexing agent. The sol stoichiometric molar ratio of Zn:Al was 1:2 and Zn:CA molar ratio was kept constant at 1:0.75. The temperature was kept at ~ 80 °C while constantly stirring the solutions using a magnetic stirrer until gels were formed. The gels were dried in an oven at 130 °C for an hour, and ground to get powders. The powders were then separated into 3 separate crucibles and annealed in a furnace at a constant temperature of 600 °C for various AT = 1, 2 and 3 h. The resulting powder products were subsequently ground using a pestle and mortar.

2.3. Characterization

The gel stretching mode frequencies were analysed by a FTIR spectrometer (Perkin Elmer). Thermogravimetric analysis of the gel was carried out using a TGA7 in the temperature range of 30-745 °C at a heating rate of 10 °C/min under an air flux. The ZnAl$_2$O$_4$ final powder products crystal structure and phase composition of the samples were characterized by powder X-ray diffraction (XRD) (Bruker AXS Discover diffractometer) with CuKα (1.5418Å) radiation. The elementary composition and surface morphology of the phosphor powders were investigated using a SEM (Shimadzu Superscan ZU SSX-550) with an energy dispersion spectroscopy (EDS). High resolution

transmission electron microscopy (HR-TEM) was performed with a JEOL JEM 2100 containing a LaB$_6$ filament. Diffuse reflectance spectra were recorded using a Lambda 950 UV-vis spectrophotometer with an integrating sphere using spectralon as a reflectance standard. Room temperature photoluminescence (PL) measurements were done using a Hitachi F-7000 fluorescence spectrophotometer.

3. Results and discussion

3.1. Fourier Transform Infrared (FTIR) and Thermogravimetric analysis (TGA) results

The FTIR spectra of the ZnAl$_2$O$_4$ gel is shown in Fig. 1 (a). The spectra show a series of absorption peaks in the range of 810 - 4000 cm^{-1}. The spectra indicate the presence of nitrates groups (at 855, 896 and 1043 cm^{-1}) [22]. The bands at 1384 and 1588 cm^{-1} can be attributed to the OH group in the metal alkoxides present in the gel [23]. The wide absorption bands centred at around 3290 cm^{-1} corresponds to OH groups, which are contributed by the water content in the sample [22,23]. The bands at 3913 and 3770 cm^{-1} are assigned to O-H stretching vibration [24].
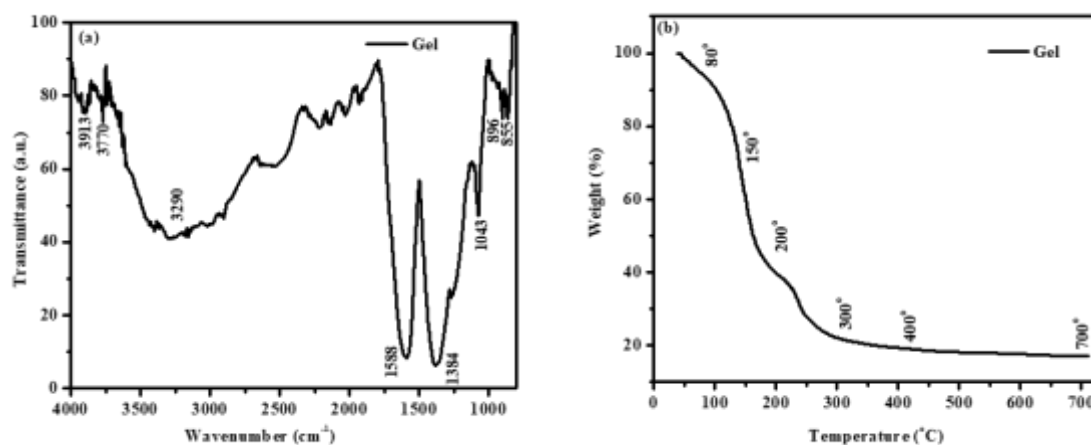

Fig. 1. (a) FTIR spectrum and (b) TGA curve of the prepared gel.

Fig. 1 (b) shows the typical thermal decomposition of the as prepared gel sample. There are three major weight loss stages observed for the prepared gel sample. The variation of the mass of the

prepared gel with increase in temperature indicates a strong loss up to 80 ^{o}C due to the release of interlayer water [25]. An event at around 150 - 200 ^{o}C, is attributed to the formation of the powder hydroxides of zinc and aluminium and expulsion of hydrated water [23]. The last event very close to 300 ^{o}C is credited to the crystallization process and the formation of single or mixed phases. Our group [19,26] have previously observed similar kind of trends in $ZnAl_2O_4$. The dehydration of residual nitrates ions are expected in the range of 177 - 400 ℃ [27]. The current results are in agreement with our previous findings [19] that the minimum annealing temperature to anticipate the $ZnAl_2O_4$ phase signature with high chances of forming other oxides such as ZnO and Al_2O_3 is 400 ^{o}C.

3.2. X-ray diffraction (XRD) properties

The obtained gel was transformed to powder via annealing at 600 ^{o}C for various hours ranging from 1 - 3 h. The XRD patterns of the powder products are presented in Fig. 2. The XRD results indicate that all of the prepared powder samples were polycrystalline. The diffraction peaks can be perfectly indexed to the mixed-phases of the face-centered cubic spinel-structured $ZnAl_2O_4$ [19,21] and hexagonal ZnO [28] respectively matching with standard diffraction data (JCPDS: 82-1043) and (JCPDS: 82-1043). The diffraction peaks and intensities of the synthesized powder and that of the standard diffraction data present quite similar behaviour. This indicates the complete formation of the mixed-phases of both cubic $ZnAl_2O_4$ and hexagonal ZnO structures under the experimental condition employed in this work [29]. On the basis of the number of the diffraction peak intensities, the ratios of 45%:55% for the $ZnAl_2O_4$/ZnO (cubic and hexagonal) phases, respectively. It is important to mention that our group [21] and Yang et al. [30] have previously reported extremely similar crystal structure consisting of both $ZnAl_2O_4$/ZnO mixed-phase. Generally, when considering the TGA results in Fig. 1 (b), it is actually possible to have the traces of impurities at the annealing temperature of 600 ^{o}C, which is also evident from the findings in Ref. [19].
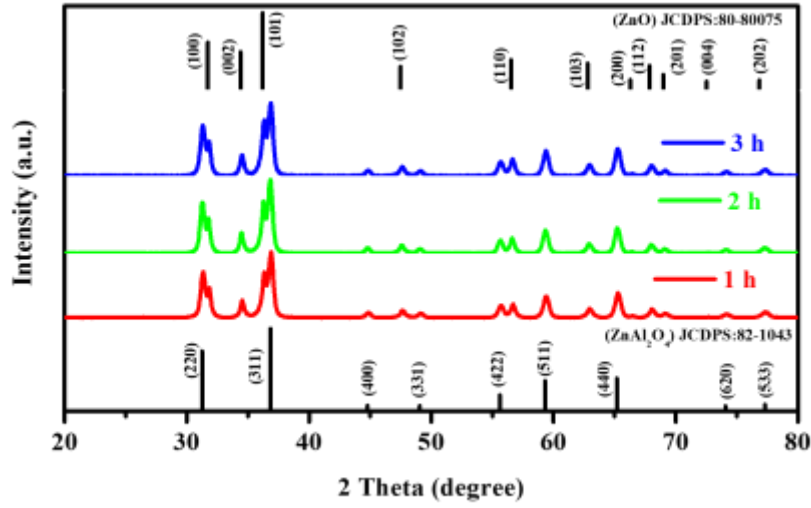
Fig. 2. XRD patterns of ZnAl$_2$O$_4$/ZnO nano-powders annealed at 600 ^{o}C for various periods.

The average crystallite size of the prepared powder samples was estimated using the Scherrer's equation [31] (Equation 1) using the most intense diffraction peaks i.e. (311) and (101) for the ZnAl$_2$O$_4$ and ZnO, respectively.

$$D = \frac{0.9\lambda}{\beta(\cos\theta)}$$

... (1)

where D is the crystallite size (nm), λ stands for the radiation wavelength (0.15406 nm), β is the full width at half maximum (radians), θ is the angle of diffraction (degrees). In order to distinguish the ZnO and ZnAl$_2$O$_4$ diffraction peaks from each other, the Gaussian fit and deconvolution of both the ZnO and ZnAl$_2$O$_4$ phases are clearly shown in Fig. 3 (a). Similar deconvolution approach as in our previous report [21] shown in Fig. 3 (a) was followed. Note that the sample annealed for 1 h was used as an example in Fig. 3 (a). The crystallite sizes of the ZnO phases were found to be 19 ± 0.3, 21 ± 1 and 19 ± 0.5 nm for the AT = 1, 2 and 3 h, respectively. The crystallite sizes of the ZnAl$_2$O$_4$ were found to be 22 ± 0.8 nm for all prepared samples. The results suggest that the AT influences the crystallite sizes of the ZnO while it does not influence the crystallites sizes of the ZnAl$_2$O$_4$. Based on

7

the fact that the most intense diffraction peak is the (311) $ZnAl_2O_4$, suggest the possibility of $ZnAl_2O_4$ quantity to be more than that of (101) ZnO. This can also be seen from the estimated average crystallites sizes (the $ZnAl_2O_4$ average crystallites are bigger than that of ZnO). Therefore, it is reasonable to conclude that the $ZnAl_2O_4$ phase exist in more proportion or quantities compared to the ZnO. That is; the ZnO serves as an impurity within the $ZnAl_2O_4$.
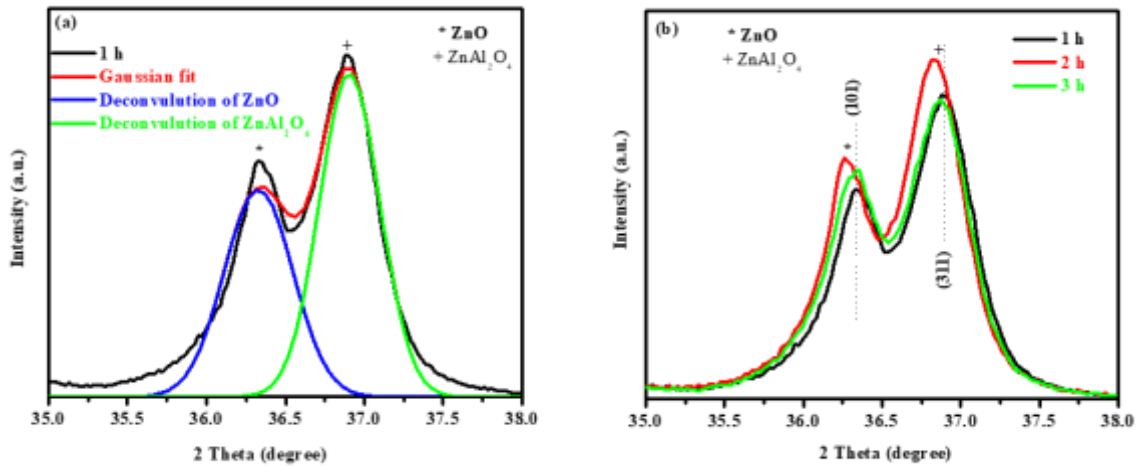

Fig. 3. (a) Deconvolution of AT = 1 h sample and (b) analysis of the most intense ZnO (101) and $ZnAl_2O_4$ (311) diffraction peaks.

From the analysis of the most intense diffraction peaks (101) and (311) shown in Fig. 3 (b), it can be seen that the crystallinity of the prepared powder samples depends on the AT. Crystallinity in this case refers to the degree of structural order in a powder samples. It is also observed that at the AT = 2 h there is a slightly shifts to the lower diffraction angle and that is attributed to the increase in the lattice parameter [32]. This phenomenon can be explained by considering the ionic radius of Zn^{2+} (0.74 Å) [18] and Al^{3+} (0.53 Å) [33] and taking into consideration that in this results, there are two mixed-phases of ZnO and $ZnAl_2O_4$. The observed behaviour might be due to many Zn^{2+} ions replacing the Al^{3+} ions in the crystal sites, which induces the population of the secondary ZnO phase to increase further. The lattice constants for the ZnO and $ZnAl_2O_4$ were calculated using Equation 2 and 3, respectively:

8

$$d_{hlk}^{ZnO} = \frac{1}{\sqrt{\dfrac{4\left(h^2 + k^2 + hk\right)}{3a^2} + \left(\dfrac{l^2}{c^2}\right)}} \qquad \dots (2)$$

$$d_{hlk}^{ZnAl_2O_4} = \frac{a}{\sqrt{\left(h^2 + k^2 + l^2\right)}} \qquad \dots (3)$$

where a and c are the lattice constants and d_{hlk} is the crystalline surface distance for hlk indices [34]. The average lattice constants of the ZnO a and c were calculated to be 3.25 and 5.20 Å, which is close to the values reported in the literature [35]. The average lattice constant for the cubic $ZnAl_2O_4$ was calculated to be $a = b = 2.43$ Å, which is similar to the value reported in our previous work [26] and the reference therein.

3.3. Morphological properties

Fig. 4 shows the EDS spectra of the prepared powder for the AT = 2 h sample. The spectra composition analyses revealed that the powder sample composed of Zn, Al and O elements. The additional peak at the lower energy ~ below 0.5 eV indicated by the star (*) is the typical carbon peak attributed to the conductive carbon (C) films coated on the sample holders during the course of EDS measurement. Apart from the anticipated elements, there were no any other extra peak/s which were detected, which indicates that the samples only consists with the Zn, Al and O. Thus, this results are in line with the TGA and XRD findings presented in Fig. 1 (b) and 2, respectively.
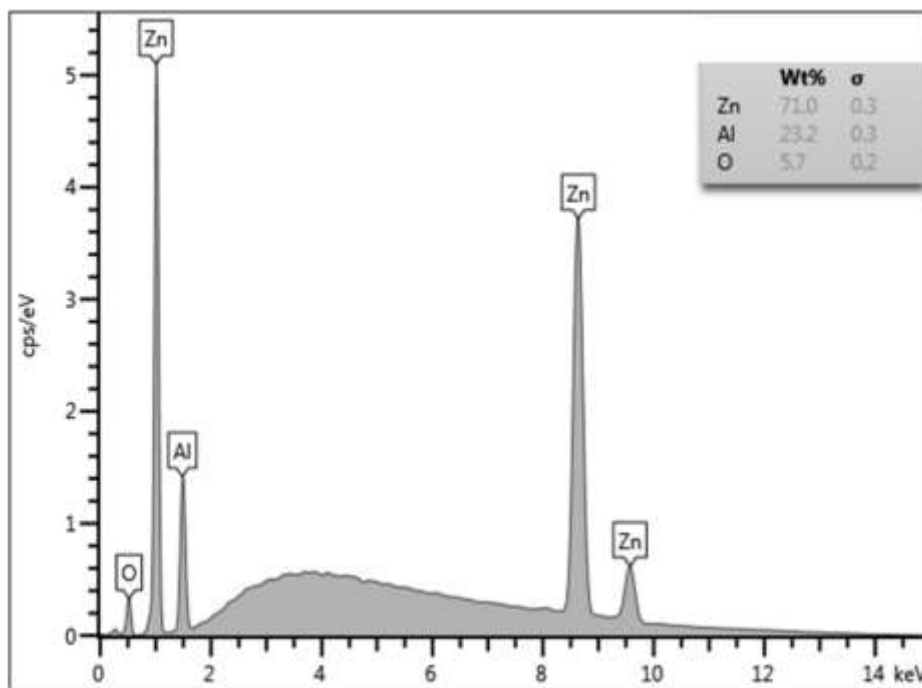
Fig. 4. EDS spectrum of the $ZnAl_2O_4$/ZnO for AT = 2 h.

The SEM was carried out in order to observe the morphologies of the obtained powder samples annealed at 600 °C for various AT's. Fig. 5 (a) shows the sample AT = 1 h and it can be observed that morphology consists of the irregular crystallites distributed over the surface. The hexagonal crystallites particles are clearly observed on the surface and based on the XRD results, this are certainly attributed to the hexagonal ZnO particles. Unfortunately, the cubic $ZnAl_2O_4$ particles were not traceable on SEM results. Few pyramid-like structures shown by the red arrows are also observed at AT = 1 h in Fig. 1 (a). These pyramid-like structures might possibly be due to the agglomeration of several hexagonal ZnO. As the AT increases to 2 h, the degree of the pyramid-like structures is more pronounced, which clearly indicated the possibilities of having more secondary hexagonal ZnO phases on the morphology as it was suggested on the XRD results for the AT = 2 h. Finally, as the AT is further increased to 3 h, the morphology seems to be returning to the one observed in Fig. 5 (a) with very few hexagonal or pyramid-like structures. Levy et al. [36] and Koao et al. [35] have previously observed similar kind of morphology as in Fig. 5 (c).

10

The prepared $ZnAl_2O_4/ZnO$ powder samples were further analysed by the HR-TEM technique. Fig. 6 (a) shows the HR-TEM image of the AT = 1 h and it can clearly be seen that the average crystallites sizes are on the nano-scale. The hexagonal ZnO structures observed in XRD and SEM results is also seen in HR-TEM results (see the insert of the zoomed version of the red highlighted section of Fig. 6 (a). The cubic-like structures shown by the red arrow is evidently observed in Fig. 6 (a) and (b). Fig. 6 (b) illustrates the HR-TEM image of the AT = 2 h. Based on the XRD results, the cubic-like structures are confidently attributed to the $ZnAl_2O_4$ crystallites. Note that Levy et al. [36] have observed similar HR-TEM results in $ZnAl_2O_4/ZnO$. Fig. 6 (c) shows the AT = 3 h sample, which also confirms that the sample is in nano-scale. Note that the 50 nm scale bar image was not visible. It is interesting to see that the XRD, SEM and HR-TEM nicely complement each other.
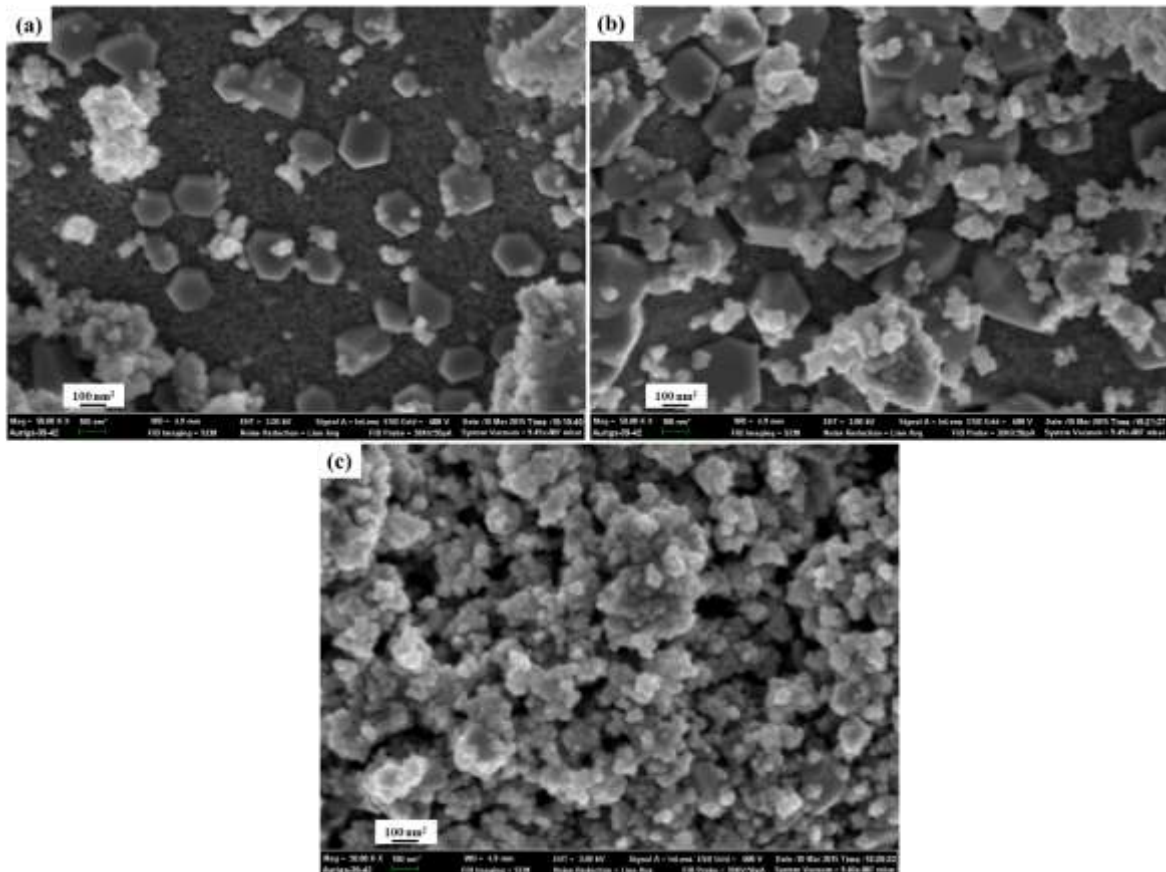

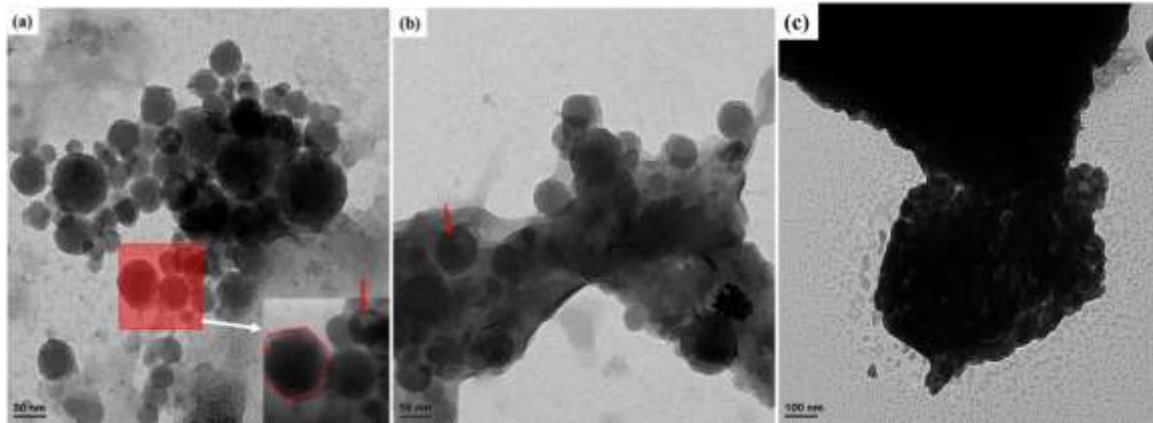**Fig. 5.** SEM images of the prepared samples for AT = (a) 1, (b) 2 and (c) 3 h.

Fig. 6. HR-TEM images of the ZnAl$_2$O$_4$/ZnO annealed for (a) 1 h (insert: higher magnification at 10 nm), (b) 2 h and (c) 3 h.

3.4. Reflectance and band gap analysis (UV-Vis Spectroscopy)

Fig. 7 (a) illustrates the UV-Vis diffused reflectance spectra of the prepared samples. The spectra revealed there is only one absorption band at around 384 nm. We have previously [19] observe this absorption band in ZnAl$_2$O$_4$. In contrast, Koao et al. [35] have also observed this absorption band in ZnO. Due to the fact that it is not an easy task to differentiate the ZnO and ZnAl$_2$O$_4$ absorption band at around 384 nm in this results. It is hence proposed that the absorption band at 384 nm be credited to both ZnO and ZnAl$_2$O$_4$ since both phases are present in this results (see the XRD, SEM and HR-TEM results). Zhang et al. [37] showed that the absorption due to the ZnAl$_2$O$_4$/ZnO combined system is around 384 nm. Furthermore, their results [37] showed that when ZnO and ZnAl$_2$O$_4$ are coupled together, the middle band gap (2.97 eV) between the conduction band (CB) bottom of the ZnO and the valence band (VB) top of ZnAl$_2$O$_4$ forms, which may be the main reason for the absorption in the visible light region.
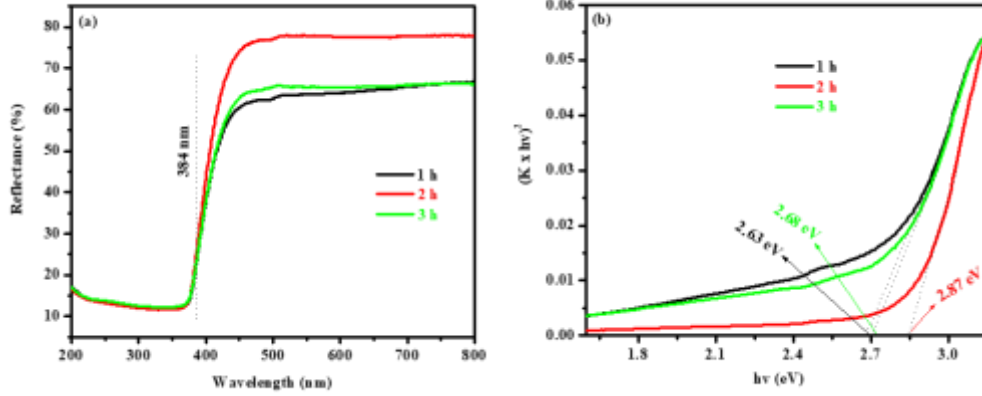
12

Fig. 7. (a) The diffuse reflectance spectra of the $ZnAl_2O_4/ZnO$ samples annealed at various AT's and (b) estimate of the direct optical band gap of the samples in (a) using Kubelka-Munk function.

The band gap energy (E_g) was calculated from the diffuse reflectance spectra by plotting the square of the Kubelka-Munk function given in Equation (4) [35]

$$K = \frac{(1-R)^2}{2R} \qquad \text{… (4)}$$

where K is reflectance transformed according to Kubelka-Munk, R is reflectance (%), h is the photon energy. In Fig. 7 (b), the E_g were measured with the help of reflectance spectra plotting graphs of $(K \times hv)^n$ versus (hv) (with $n = 2$, which is appropriate for a direct band gap material such as $ZnAl_2O_4$). The extrapolation of linear region of this plot to $(K \times hv)^2 = 0$ gives the direct band gap value. The E_g value for the AT = 1, 2 and 3 h were respectively found to be 2.63, 2.87 and 2.68 eV, which is consistence with the literature values by other researchers [37]. The optical E_g is observed to increases and then decreases with the increasing AT. We propose that this behaviour might be due to the fluctuation on the crystallites sizes of the ZnO as observed on the XRD results. Thus, the results suggest that the E_g of the prepared samples $ZnAl_2O_4/ZnO$ can be tuned by varying the AT.

13

3.5. Photoluminescent (PL) analysis

PL excitation and emission spectrum of the $ZnAl_2O_4$/ZnO nano-powders synthesized at different AT is shown in Fig. 8. The excitation spectra were recorded when monitoring an emission at 428 nm. There is one major peaks located at 275 nm which is attributed to the band-to-band direct excitation in $ZnAl_2O_4$ [21]. The emission spectra of these samples, taken under the excitation at 275 nm shows two emissions peaks located around 428 and 561 nm. These emission peaks can be ascribed to be due to both contribution of ZnO and $ZnAl_2O_4$ intra band gap defects such as oxygen vacancies (V_0^*) [8,21,38-40], which is quite reasonable when considering the fact that the presence of oxygen was evidently detected by the EDS in Fig. 4. For the investigated range of AT = 1 - 3 h, the sample AT = 2 h had the highest emission intensity. The proposed explanation for this behaviour is that the emission channel for this sample is originating from both $ZnAl_2O_4$ and many ZnO as it was shown on the XRD and SEM results that the ZnO particle are populating more at AT = 2 h compared to the other samples. Therefore, the results suggest that the AT have the influence on the structural and morphological changes, which considerably influence the PL emission intensity. Similar study [41] in $MgAl_2O_4$:0.3% In^{3+} has also confirmed that the AT significantly influences the emission intensity. The Gaussian fit showed that the optimum AT on the $MgAl_2O_4$:0.3% In^{3+} system was AT = 2.3 h.

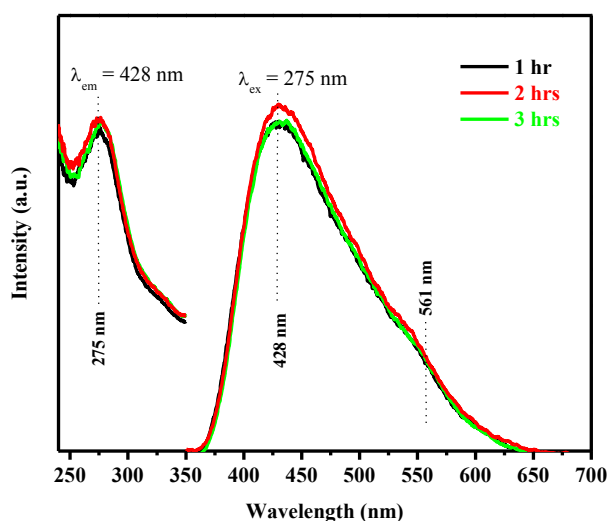**Fig. 8.** (a) The excitation and emission spectra of the $ZnAl_2O_4$/ZnO samples annealed at various periods.

14

In order to explain the dynamics behind the PL excitation and emission pathways or mechanism of the prepared $ZnAl_2O_4$/ZnO samples, it is necessary to propose a schematic band diagram to demonstrate all of the processes associated with the excitation and emission for the system. Fig. 9 illustrates the schematic band diagram for the PL pathways of $ZnAl_2O_4$/ZnO samples. Assuming that the E_g of the $ZnAl_2O_4$ is ~ 3.8 eV [7,8], it is clear that when the samples are excited with light of wavelength 275 nm (~ 4.5 eV), the electrons (shown by the red shaded cycles in Fig. 9) in the valence band (VB) are excited and trapped into the conduction band (CB) of the $ZnAl_2O_4$. Taking into account the E_g of the $ZnAl_2O_4$ and ZnO (~ 3.4 eV) [40], it is possible to have the CB of ZnO in the same level as that one of $ZnAl_2O_4$. In that case the VB of ZnO will be within the $ZnAl_2O_4$ E_g and the electron can then be excited into the ZnO CB. In addition, it is also possible to find both the VB and CB of ZnO within the E_g of the $ZnAl_2O_4$. Thus, it is clear that the ZnO is an impurity in $ZnAl_2O_4$, which serves as the dopant or trapping centre of the de-excited electron. Based on the proposed pathways shown in Fig. 9, it is therefore emphasized that the excited electrons are trapped into the CB of $ZnAl_2O_4$ not the CB of ZnO. The excited electrons are de-excited by non-radiative relaxation (NRR) via different channels as shown in Fig. 9 and gets trapped on the defects states in either $ZnAl_2O_4$ or ZnO. These electrons are then further de-excited from the trap level to either another trap level (via NRR) or to the VB (via radiative decay), in case of $ZnAl_2O_4$, which results in the observed emissions colours as shown in Fig. 9. Depending on the electrons de-excitation channel, it is quite clear that both emissions peaks at 428 and 561 nm can originate either in $ZnAl_2O_4$ or ZnO. All of the emissions coming from the $ZnAl_2O_4$ are attributed to the radiative decay, which are due to the electron (from different trap levels as shown in Fig. 9) recombination with a hole in the VB [8]. On the other hand, ZnO is composed of extrinsic and intrinsic deep level defects that emit different colours in the visible region [42]. The various defects such as oxygen vacancies (V_o), zinc vacancies (V_{zn}), oxygen interstitial (O_i), zinc interstitial (Zn_i), and anitisite oxygen (O_{zn}) arising are the reason behind the deep level emission at visible range. The emissions from the ZnO at 428 nm is ascribed to the transition energy from Zn_i to VB in ZnO [42]. The presence of green emission 561 nm in ZnO is ascribed to the oxygen vacancies (V_o) [39,42,43]. It is crucial to note that these emissions from $ZnAl_2O_4$ and ZnO at 428 and 561 nm cannot be differentiated. Thus, we infer that they originate or

they are observed due to the contribution of both ZnO and $ZnAl_2O_4$ as per proposed pathways shown in Fig. 9.
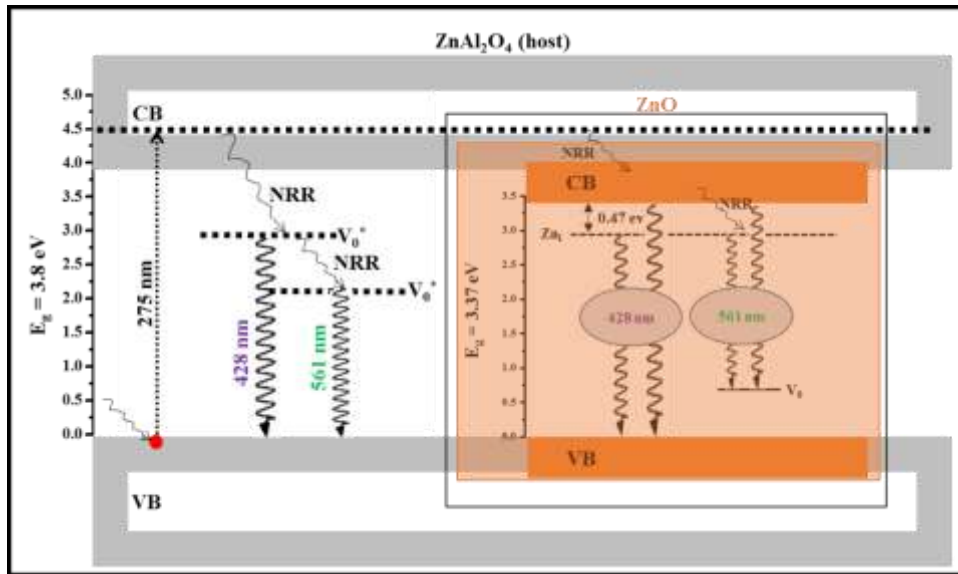

Fig. 9. The proposed emission pathways in $ZnAl_2O_4/ZnO$.

The dependency of the emission wavelength to the excitation wavelength was investigated on the samples AT = 2 h. For the samples were excited at various wavelengths as shown in Fig. 10 (a). When the excitation wavelength is increased (in steps of 10 nm from 270 to 310 nm), the violet emission slightly shifts from 430 to 440 nm. For the excitation at 250 nm there seems to be emission peak at 553 nm. The emission intensity as a function of the excitation wavelength is shown in Fig. 10 (b). The Gaussian fit indicates that 275 nm is the dominant excitation with the highest emission intensity. This is the main reason why the samples shown in Fig. 8 were excited at 275 nm. In Fig. 10 (a), the violet (430 to 440 nm) and green (553 nm) emission peaks are certainly attributed to originate from the ZnO and $ZnAl_2O_4$ as discussed above (see Fig. 9) [8,42,43].
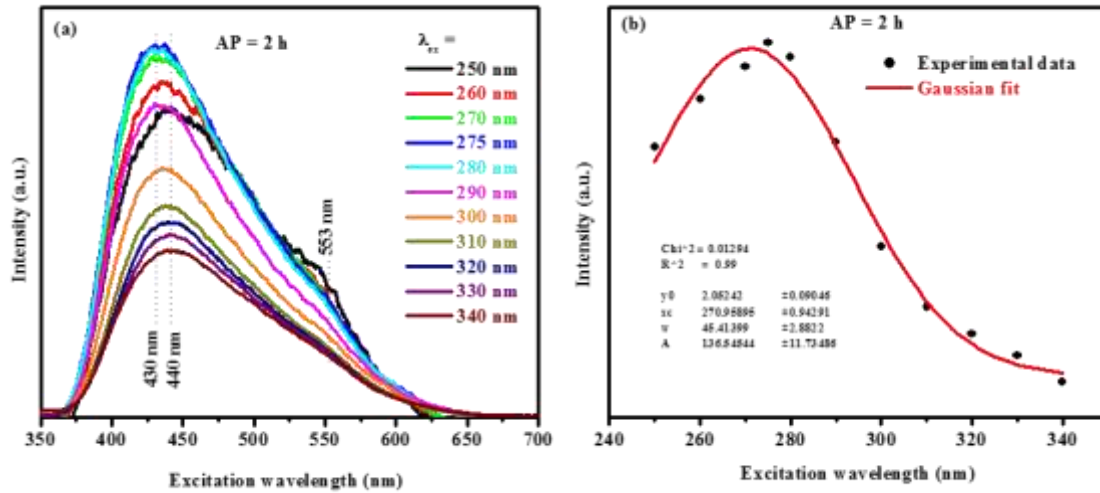
Fig. 10. (a) Sample (AT = 2 h) at different excitations wavelengths and (b) the emission intensity as a function of the excitation wavelength.

3.7. Colour coordinates analysis

The International Commission on Illumination (CIE) chromaticity diagram and coordinates for the $ZnAl_2O_4/ZnO$ samples at different AT and for the sample AT = 2 h excited at various wavelength are shown in Fig. 11 (a) and (b), respectively. Generally and as anticipated from the PL results in Fig. 10 (a)), it can be seen that the emission colour cannot be tuned by varying the AT and excitation wavelength. These results are similar to our previous results on the $MgAl_2O_4$:0.33% In^{3+} system [43]. On the other hand, our group [44] have previously observed the possibility of tuning the emission colour by varying the excitation wavelength due to the change of the emission centres. Furthermore, the results [44] also showed that the emission colour can be tuned by varying the x% Tb^{3+} and the excitation wavelength.
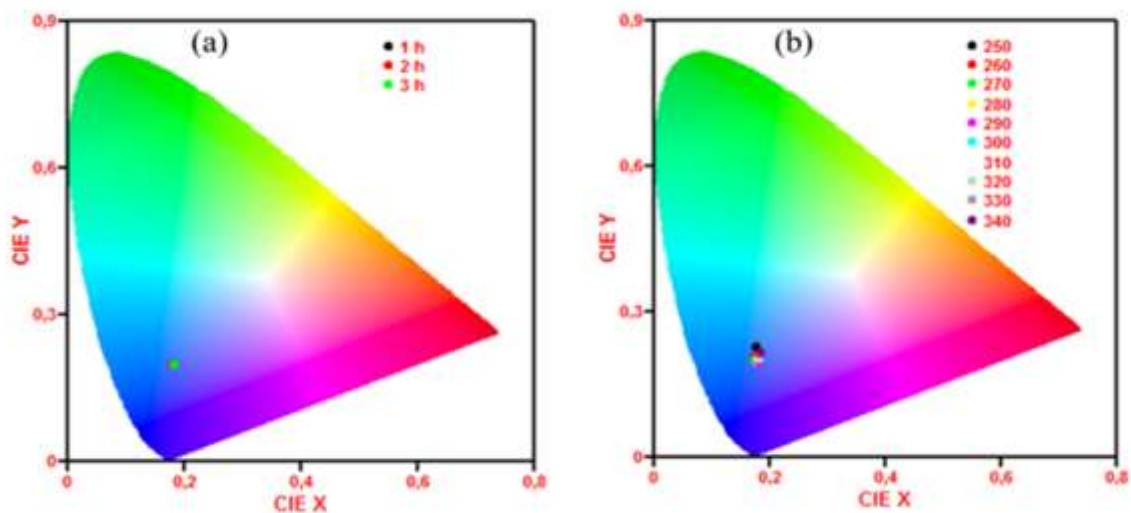
Fig. 11. CIE chromaticity co-ordinates for the $ZnAl_2O_4$/ZnO samples (a) annealed at various periods and (b) AT = 2 h at different excitation wavelength.

4. Conclusion

$ZnAl_2O_4$ nano-powders with ZnO impurities have been successfully prepared via citrate sol-gel technique. TGA analysis revealed that the minimum annealing temperature of crystallization was ~ 400 °C. XRD, SEM and HR-TEM analysis confirmed that all of the prepared nano-powders consisted of the mixture of cubic $ZnAl_2O_4$ and hexagonal ZnO structures. The morphology of the prepared nano-powders was influenced by the AT. The PL results showed that the violet (428 nm) and green (561 nm) emissions were due to both contribution from the $ZnAl_2O_4$ and ZnO. The CIE colour coordinates showed that the emission colour cannot be tuned by varying the AT.

Acknowledgements

18

References

[1] L. Cornu, M. Dutttine, M. Gaudon, V. Jubera, Luminescence switch of Mn-doped $ZnAl_2O_4$ powder with temperature, J. Matter. Chem. C. 2 (2014) 9512-9522.

[2] L.H. Ha, P.T. Lanh, N.N. Long, T.T. Loan, Some physical properties of $ZnAl_2O_4$:Cr^{3+} (Co^{2+}) powders prepared by hydrothermal method, J. Phys. Conf. Ser. 187 (2009) 012053.

[3] F.M. Stringhini, E.L. Foletto, D. Sallet, D.A. Bertuol, O. Chiavone-Filho, C.A. Oller do Nascimento, Synthesis of porous zinc aluminate spinel ($ZnAl_2O_4$) by metal-chitosan complexation method, J. Alloys Compd. 588 (2014) 305-309.

[4] N. Pathak, S.K. Gupta, K. Sanyal, M. Kumar, R.M. Kadam, V. Natarajan, Photoluminescence and EPR studies on Fe^{3+} doped $ZnAl_2O_4$: an evidence for local site swapping of Fe^{3+} and formation of inverse and normal phase, Dalton Trans. 43 (2014) 9313-9323.

[5] R. Roesky, J. Weiguny, H. Bestgen, U. Dingerdissen, An improved synthesis method for indenes and styrenes by use of a ZnO/Al_2O_3 spinel catalyst, Appl. Catal. A Gen. 176 (1999) 213-220.

[6] W. Strek, P. Deren, E. Lukowiak, B. Nissen, J. Wrzyszcz, M. Zawadzki, P. Pershukevich, Preparation and emission spectra of Eu(III) in nanostructured γ-alumina, Spectrochim. Acta A 54 (1998) 2121-2124.

[7] E.L. Foletto, S. Battiston, J.M. Simões, M.M. Bassaco, L.S.F. Pereira, E.M. de Moraes Flores, E.I. Müller, Synthesis of $ZnAl_2O_4$ nanoparticles by different routes and the effect of its pore size on the photocatalytic process, Microporous Mesoporous Mater. 163 (2012) 29-33.

[8] S-F. Wang, G-Z. Sun, L-M. Fang, L. Lei, X. Xiang, X-T. Zu, Synthesis and photoluminescence characteristics of Dy^{3+}-doped $ZnAl_2O_4$ nanocrystals via a combustion process, Sci. Rep. 5 (2015) 12849.

[9] M-T. Tsai, Y-X. Chen, P-J. Tsai, Y-K. Wang, Luminescent and structural properties of manganese-doped zinc aluminate spinel nanocrystals, Thin Solid Films 518 (2010) e9-e11.

[10] S.F. Wang, F. Gu, M.K. Lu, X.F. Cheng, W.G. Zou, G.J. Zhou, S.M. Wang, Y.Y. Zhou, Synthesis and photoluminescence characteristics of Dy^{3+}-doped $ZnAl_2O_4$ nanocrystals via a combustion process, J. Alloys Compd. 394 (2005) 255-258.

[11]T.K. Parya, R.K. Bhattacharyya, S. Banerjee, U.B. Adhikari, Co-precipitated $ZnAl_2O_4$ spinel precursor as potential sintering aid for pure alumina system, Ceram. Int. 36 (2010) 1211-1215.

[12]L. Chen, X. Sun, Y. Liu, K. Zhou, Y. Li, Porous $ZnAl_2O_4$ synthesized by a modified citrate technique, J. Alloys Comp. 376 (2004) 257-261.

[13]M. Zawadzki, Synthesis of nanosized and microporous zinc aluminate spinel by microwave assisted hydrothermal method (microwave-hydrothermal synthesis of $ZnAl_2O_4$), Solid State Sci. 8 (2006) 14-18.

[14]L. Zou, F. Li, X. Xiang, D.G. Evans, X. Duan, Self-generated Template Pathway to High-Surface-Area Zinc Aluminate Spinel with Mesopore Network from a Single-Source Inorganic Precursor, Chem. Mater. 18 (2006) 5852-5859.

[15]Z. Zhu, X. Li, Q. Zhao, S. Liu, X. Hu, G. Chen, Facile solution synthesis and characterization of porous cubic-shaped superstructure of $ZnAl_2O_4$, Mater. Lett. 65 (2011) 194-197.

[16]M.T. Tsai, Y.S. Chang, I.B. Huang, B.Y. Pan, Luminescent and structural properties of manganese-doped zinc aluminate spinel nanocrystals, Ceram. Int. 39 (2013) 3691-3697.

[17]L. Gama, M.A. Ribeiro, B.S. Barros, R.H.A. Kiminami, I.T. Weber, A.C.M. Costa, Synthesis and characterization of the $NiAl_2O_4$, $CoAl_2O_4$, and $ZnAl_2O_4$ spinels by the polymeric precursors method, J. Alloy Comp. 483 (2009) 453-455.

[18]B. Cheng, S. Qu, H. Zhou, Z. Wang, Porous $ZnAl_2O_4$ spinel nanorods doped with Eu^{3+}: synthesis and photoluminescence, Nanotechnology 17 (2006) 2982-2987.

[19]S.V. Motloung, M. Tsega, F.B. Dejene, H.C. Swart, O.M. Ntwaeaborwa, L.F. Koao, T.E. Motaung, M.J. Hato, J. Alloy Comp. 677 (2016) 72-79.

[20]L. Cornu, M. Gaudon, V. Jubera, J. Mat. Chem. C 1 (2013) 5419-5428.

[21]S.V. Motloung, F.B. Dejene, H.C. Swart, O.M. Ntwaeaborwa, J. Lumin.163 (2015) 8-16.

[22]W.X. Kuang, Y.N. Fan, K.W. Yao, Y. Chen, J. Solid State Chem. 140 (1998) 354-360.

[23]E.M.A. Jamal, D.S. Kumar, M.R. Anantharaman, Bull. Mater. Sci. 34 (2011) 251-259.

[24]A.K. Bajpai, S. Likhitkar, Bull. Mater Sci. 36 (2001) 15-24.

[25]X. Wei, D. Chen, Mater. Lett 60 (2006) 823-827.

[26] S. V. Motloung, F.B. Dejene, H.C. Swart, O.M. Ntwaeaborwa, Effect of annealing temperature on structural and optical properties of $ZnAl_2O_4$:1.5% Pb^{2+} nanocrystals synthesized via sol-gel reaction, J. Sol-Gel Sci. Technol. 70 (2014) 422-427.

[27] L.F. Koao, B.F. Dejene, H.C. Swart, S.V. Motloung, T.E. Motaung, S.P. Hlangothi, Effect of Tb^{3+} ions on the ZnO nanoparticles synthesized by chemical bath deposition method, Adv. Mater. Lett. 2016, **7**(7), 529-535.

[28] N.A.K. Aznan, M.R. Johan, Quantum Size Effect in ZnO Nanoparticles via Mechanical Milling, J. Nanomater. 2012 (2011) 1-4.

[29] S. Battiston, C. Rigo, E. da Cruz Severo, M.A. Mazutti, Synthesis of Zinc Aluminate ($ZnAl_2O_4$) Spinel and Its Application as Photocatalyst, Mater. Res. 17 (3) (2014) 734-738.

[30] M. Yang, S. Li, G. Chen, High-temperature steam reforming of methanol over $ZnO-Al_2O_3$ catalysts, Appl. Catal. B: Environ. 101 (2011) 409-416.

[31] B.D. Cullity, S.R. Stock, Elements of X-ray Diffraction, third ed., Prentice Hall Publishers, New Jersey, (2001).

[32] L.F. Koao, B.F. Dejene, R.E. Kroon, H.C. Swart, Effect of Eu^{3+} on the structure, morphology and optical properties of flower-like ZnO synthesized using chemical bath deposition, J. Lumin. 147 (2014) 85-89.

[33] I. Miron, I. Grozescu, Hydrothermal synthesis of $ZnAl_2O_4$:Cr^{3+} nano-crystals, Optoelect. Adv. Mat. 6 (2012) 673-675.

[34] S. Iaiche, D. Djelloul, $ZnAl_2O_4$/ZnO Nanocomposite Films Studied by X-Ray Diffraction, FTIR, and X-Ray Photoelectron Spectroscopy, J. Spectrosc. 2015 (2015) 1-9.

[35] L.F. Koao, F.B. Dejene, M. Tsega, H.C. Swart, Annealed Ce^{3+}-doped ZnO flower-like morphology synthesized by chemical bath deposition method, Physica B 480 (2016) 53-57.

[36] C. Levy, M. Watanabe, Y. Aizawa, H. Inomata, Synthesis of Nanophased Metal Oxides in Supercritical Water: Catalysts for Biomass Conversion, Int. J. Appl. Ceram. Technol. 3 [5] (2006) 337-344.

[37] L. Zhang, J-H. Yan, M-J. Zhou, Y-p. Yu, Y. Liu, Y-n Liu, Photocatalytic degradation and inactivation of Escherichia coli by $ZnAl_2O_4$/ZnO with heteronanostructures, Trans. Nonferrous Met. Soc. China 24 (2014) 743-749.

[38] A.A. Da Silva, A. Goncalves, M.R. Davolos, S.H. Santagneli, Al^{3+} Environments in Nanostructured $ZnAl_2O_4$ and Their Effects on the Luminescence Properties, J. Nanosci. Nanotechnol. 8 (2008) 5690-5695(6).

[39] A.A. Da Silva, A. Goncalves, M.R. Davolos, Characterization of nanosized $ZnAl_2O_4$ spinel synthesized by the sol-gel method, J. Sol-Gel Sci. Technol. 49 (2009) 101-105.

[40] M. Willander, O. Nur, N. Bano, K. Sultana, Zinc oxide nanorod-based heterostructures on solid and soft substrates for white-light-emitting diode applications, New J. Phys. 11 (2009) 125020 (16pp).

[41] L.T. Melato, T.E. Motaung, O.M. Ntwaeaborwa, S.V. Motloung, Effect of annealing at different time intervals on the structure, morphology and luminescent properties of $MgAl_2O_4$:0.3% In^{3+} nanophosphor prepared by citrate sol-gel method, Opt. Mater. 66 (2017) 319-326.

[42] R. Amiruddin, M.C.S. Kumar, Enhanced visible emission from vertically aligned ZnO nanostructures by aqueous chemical growth process, J. Lumin. 55 (2014) 149-155.

[43] S. Mehmood, M.A. Rehman, H. Ismail, B. Mirza, A.S. Bhatti, Significance of postgrowth processing of ZnO nanostructures on antibacterial activity against gram-positive and gram-negative bacteria, Int. J. Nanomedicine 10 (2015) 4521-4533.

[44] S.V. Motloung, B.F. Dejene, O.M. Ntwaeaborwa, H.C. Swart, R.E. Kroon, Colour tuning and energy transfer pathways in $MgAl_2O_4$ triply doped with 0.1% Ce^{3+}, 0.1% Eu^{2+}, x% Tb^{3+} $\left(0 \leq x \leq 2\%\right)$ nanocrystals synthesized using sol-gel process, Chem. Phys. 487 (2017) 75-86.